Modeling glenohumeral stability in musculoskeletal simulations
A validation study with in vivo contact forces

Hasan, Ibrahim Mohammed I.; Belli, Italo; Seth, Ajay; Gutierrez-Farewik, Elena M.

DOI
10.1109/TNSRE.2025.3635012

Publication date
2025

Document Version
Final published version

Published in
IEEE Transactions on Neural Systems and Rehabilitation Engineering

Citation (APA)
Hasan, I. M. I., Belli, I., Seth, A., & Gutierrez-Farewik, E. M. (2025). Modeling glenohumeral stability in musculoskeletal simulations: A validation study with in vivo contact forces. *IEEE Transactions on Neural Systems and Rehabilitation Engineering*, *33*, 4657-4668. https://doi.org/10.1109/TNSRE.2025.3635012

Modeling Glenohumeral Stability in Musculoskeletal Simulations: A Validation Study With In Vivo Contact Forces

Ibrahim Mohammed I. Hasan, Italo Belli, Ajay Seth, and Elena M. Gutierrez-Farewik, *Member, IEEE*

***Abstract*— Common optimization approaches for solving the muscle redundancy problem in musculoskeletal simulations can predict shoulder contact forces that either violate or barely satisfy joint stability requirements, with force directions falling outside or near the perimeter of the glenoid cavity. In this study, several glenohumeral stability formulations were tested against *in vivo* measurements of glenohumeral contact forces from the *Orthoload* dataset on one participant data in lateral, posterior, and anterior dumbbell raises. The investigated formulations either constrained the contact force direction to remain within different shapes of a stability perimeter, or added a penalty term that discouraged contact force directions from deviating from the glenoid cavity center. All stability formulations predicted contact force magnitudes that agreed relatively well to the *in vivo* measured forces except for the strictest formulation that constrained the joint contact force directly to the glenoid cavity center. Constraint and conditional penalty models estimated force vectors that largely lay along the perimeters. Continuous penalty models estimated relatively more accurate contact force directions within the glenoid cavity than constraint models. Our findings support the proposed penalty formulations as more reasonable and accurate than other investigated existing glenohumeral stability formulations.**

***Index Terms*— Shoulder loading, shoulder stability, biomechanical simulations.**

I. Introduction

THE shoulder has the greatest range of motion in the human body, but is particularly prone to injuries in the glenohumeral (GH) joint [1], [2]. The GH joint is often considered as a ball-and-socket joint, but the socket, or the glenoid fossa of the scapula, is relatively shallow and small, covering at most only a third of the ball, or the head of the humerus [3]. Without surrounding bony cover to provide stability, GH stability is attained passively through glenoid concavity, the glenoid labrum surrounding the glenoid fossa, the joint capsule, ligaments and passive muscle tension, and actively through muscle contraction [4]. Any compromise in these stabilizing elements can lead to excessive humeral head translation and joint luxation, with increased risk of injury and pain [5]. Understanding joint stability is thus essential for preventing and mitigating shoulder injuries.

GH stability can be mechanically characterized by the magnitude and direction of the glenohumeral joint contact force (GH-JCF) vector. GH-JCF is the net sum of internal and external forces acting on the joint. The stability limit was introduced as a metric to quantify physical limits of GH stability [6], [7]. Stability limits were obtained experimentally via *in vitro* cadaver concavity compression tests wherein the humeral head was compressed into the glenoid cavity with a known force and shear force was applied perpendicularly until the humeral head was dislocated. The stability limit is defined as the magnitude ratio between the component of the GH-JCF that can translate the humeral head out of the glenoid cavity and the compressive component, which pushes the humeral head into the glenoid cavity. Higher stability limit in a given direction indicates a relatively more GH stability in that direction. If the stability limit is exceeded, the contact force vector will be directed outside the edge of the glenoid cavity, leading to joint dislocation. Empirical stability limits were reported as highest in the superior direction (≈ 0.60) and lowest in the anterior (≈ 0.32) direction with the glenoid labrum intact [7], indicating that GH joint is more stable in the superior-inferior direction than in the anterior-posterior direction.

Quantitative analysis of GH stability is contingent on the availability of either measurements or estimations of GH-JCFs. Previously, GH-JCFs were measured experimentally using instrumented shoulder prostheses, but that has limited feasibility when shoulder replacement surgeries are planned [8], [9], [10]. Alternatively, GH-JCFs can be quantified by measuring forces in the structures that create the contact forces, including all muscles. Measuring activation of superficial muscles,

Received 19 May 2025; revised 26 September 2025; accepted 17 November 2025. Date of publication 19 November 2025; date of current version 27 November 2025. This work was supported in part by the Promobilia Foundation under Grant 18200, Grant 23300, and Grant A23165; and in part by Swedish Research Council under Grant 2018-00750. *(Corresponding author: Ibrahim Mohammed I. Hasan.)*

Ibrahim Mohammed I. Hasan is with the KTH MoveAbility, Department of Engineering Mechanics, KTH Royal Institute of Technology, 100 44 Stockholm, Sweden (e-mail: imihasan@kth.se).

Italo Belli is with the Biomechanical Engineering Department and the Department of Cognitive Robotics, Delft University of Technology, 2628 CD Delft, The Netherlands (e-mail: i.belli@tudelft.nl).

Ajay Seth is with the Biomechanical Engineering Department, Delft University of Technology, 2628 CD Delft, The Netherlands (e-mail: a.seth@tudelft.nl).

Elena M. Gutierrez-Farewik is with the KTH MoveAbility, Department of Engineering Mechanics, KTH Royal Institute of Technology, 100 44 Stockholm, Sweden, and also with the Department of Women's and Children's Health, Karolinska Institute, 171 77 Stockholm, Sweden (e-mail: lanie@kth.se).

Digital Object Identifier 10.1109/TNSRE.2025.3635012

e.g. deltoids, biceps and triceps, is easy to perform experimentally using surface electromoygraphy (EMG), however measuring activation of deep muscles, including rotator cuff muscles, would require extensive invasive fine-wire EMG measurements [11] which is experimentally difficult. Subsequent mapping of EMG measurements into muscle forces is furthermore still a major challenge [12].

Musculoskeletal modeling is an alternative approach to estimate muscle, ligament, and joint contact forces that are difficult to measure experimentally. Several shoulder musculoskeletal models exist and have been used to study shoulder biomechanics [13], [14], [15], [16], [17], [18], [19], [20]. These models have been used to provide insights on shoulder loading in different applications, such as tendon transfer surgery [21], shoulder implants [22], and wheelchair propulsion [20], [23]. However, they have oversimplified the complex multibody geometry and articulations, specifically by ignoring [24] or inaccurately estimating the articulation of the scapula over the thorax [25], [26]. To address some of these shortcomings, a recently developed *OpenSim* shoulder model provided a novel formulation for scapulothoracic articulation that was validated with bone-pin kinematic measurements and shown to be robust for noisy marker tracking [27]. An enhanced version of this model, the thoracoscapular model, included several shoulder muscles such as the rotator cuff muscles and was used to study muscle work in typical shoulder movement such as shoulder shrugging, lateral arm raise, and anterior arm raise [28], with muscle redundancy solved via the Computed Muscle Control algorithm [29].

In musculoskeletal simulations, the muscle redundancy problem has historically been addressed as an optimization problem that seeks a solution that satisfies a specified criterion measure and a set of imposed constraints. Frequently used criterion measures include minimum sum of muscle stresses [17], [30], muscle metabolic rates [30], or muscle activations [11], [16]. Unrealistic solutions to the muscle redundancy problem may arise if GH stability is not properly addressed [17], [25], [31], [32]. Theoretically, models that minimize summed muscle activations or effort while allowing joint reaction forces in any direction are likely to underestimate co-contraction, particularly that of the rotator cuff muscles, which serves to ensure that the humeral head articulates with the glenoid [1], [33], [34].

GH stability has been formulated as an inequality constraint that restrains the direction of the joint contact force to lie within a specified perimeter that describes the glenoid cavity, which has been estimated with different geometric shapes, including an ellipse [11], [13], [14], [34], a circle [35] and a polynomial [31]. The circle model assumes that the GH stability is radially symmetric around the cavity center. The ellipse model considers the spatial variation of the stability limit, with its major axis aligning with the superior-inferior direction and its minor axis aligning with the posterior-anterior direction. The polynomial formulation also accounts for spatial variability. It was derived empirically from concavity compression tests [6] as a set of polynomial functions that fit eight discrete points along the glenoid border [17], [31].

A rapid muscle redundancy (RMR) solver was recently developed to solve the load sharing problem in the thoracoscapular model [33]. The RMR solver adopted a stability model that approximated the stability border as a circle, and estimated higher activation of the rotator cuff muscles than without any constraint, suggesting more reasonable active contribution of the rotator cuff muscles to GH stability. The GH-JCF vector, however, was frequently directed along the circular perimeter, as this was the "cheapest" solution. This finding raises questions to its validity in predicting muscle activity.

Instead of inequality constraint formulations that force the joint contact force to be directed within a specified area, a different strategy to model GH stability was presented by introducing a conditional penalty to the objective function that triggers if the GH-JCF direction crossed a specified stability perimeter [36]. The penalty term was proportional to the squared distance that the GH-JCF direction deviated outside the perimeter. This formulation, however, often estimated GH-JCFs that were directed along or occasionally outside the stability perimeter.

Several knowledge gaps exist with the current stability formulations. The existing inequality constraint models approximate the stability perimeter differently, and there is no clear evidence on which model is most reasonable. For most formulations, the directions of the estimated joint contact forces were evaluated and considered plausible if they fell within the perimeter, but were not compared to gold standard *in vivo* measurements. The exception to this is the ellipse model implemented into the Delft shoulder model, for which computed GH-JCFs were tested against *in vivo* measurements from the *Orthoload* dataset [37]. The model reproduced the direction of the GH-JCF inside the glenoid cavity. Discrepancies were, however, present between the measured and estimated GH-JCF magnitudes, specifically for dynamic tasks above 90^o of shoulder elevation, which the authors attributed to the inability of the model to reproduce co-contraction [37]. Implemented in a different shoulder model, the ellipse formulation was also shown to underestimate co-contraction of the rotator cuff muscles compared to *in vivo* fine-wire EMG measurements [11]. GH-JCF magnitudes computed using the AnyBody shoulder model were also compared to in vivo measurements [38], [39]. In these studies force dependent kinematics approach was used to estimate shoulder loading while ensuring GH stability. In another study using the Anybody shoulder model, estimated glenohumeral contact forces were compared with in vivo measurements [20], but contact force directions were not assessed, and it was not clear whether a stability formulation was used. Contact force direction is likely sensitive to the glenohumeral stability model [31], [32], and the extent to which those results reflect accurate directional predictions remains uncertain.

The objectives of this study were to determine how different formulations of GH stability in musculoskeletal simulation influence estimated GH-JCF magnitude and direction, in relation to reported *in vivo* joint contact force measurements, and to evaluate how rotator cuff muscles co-contraction was predicted with the different stability formulations.

II. Materials and Methods

We performed musculoskeletal simulations on the experimental data available from the *Orthoload* dataset. In the thoracoscapular model, joint angles, velocities and accelerations were computed via inverse kinematics. Muscle redundancy was then solved with the RMR solver repeatedly, for several different joint stability formulations that constrain the direction of the GH-JCF; these include constraining the stability perimeter as different shapes, then by penalizing joint contact force directions outside of a defined perimeter. Estimated joint contact force magnitude and direction were compared with *in vivo* measurements.

A. Orthoload Dataset

Available *Orthoload* data from subject S8R with an instrumented hemiarthroplasty in the right shoulder (male, 74 y, mass 83 kg, height 173 cm) was used in this study [8], [9], [10]. The subject had previously undergone joint hemiarthroplasty with a delto-pectoral approach with no observed nerve or rotator cuff damage. The subject performed three tasks: lateral raise (abduction), posterior raise (backward flexion), and anterior raise (forward flexion) with a 2.4 kg handheld dumbbell [10]. Kinematic data had been measured with marker clusters placed on thorax, scapula (on the acromion), upper arm, and forearm using Optotrak motion capture system (Northern Digital Inc., Canada) cameras at a sampling frequency of 50 Hz. Bony landmarks of the scapula: Angulus Acromialis, Trigonum Spinae, and Angulus Inferior were identified in calibration trials using a scapula locator [40], and constructed in dynamic trials from the acromion cluster. GH-JCFs were measured with the instrumented joint prothesis that sent data wirelessly to an external measuring system and resampled to 50 Hz. Forces were measured in the instrumented joint prosthesis coordinate frame of reference. A coordinate transformation from the prothesis frame to the local coordinate system of the glenoid cavity was then obtained from subject-specific computed tomography images of the participant [10].

B. Musculoskeletal Model

The thoracoscapular model consists of a multibody chain that defines articulation among right upper body clavicle, scapula, humerus, ulna, and radius [28]. A closed chain mechanism is formed with a 4 degree-of-freedom (DoF) scapulothoracic *OpenSim* mobilizer [27], a 2 DoF joint between the thorax and clavicle, and a joint between the clavicle and the acromion that allows 3D rotation but no translation. The GH joint is modeled as a spherical joint with 3 rotational DoFs, i.e., no translation is allowed, according to the ISB standard [41]. The elbow is modeled as a 1 DoF rotational joint, and the forearm with a 1 DoF rotational joint between the ulna and radius to model forearm pronation/supination. The hand is rigidly fixed to the radius and the whole multibody chain is anchored to the ground via a 6 DoF joint at the thorax. The model includes 33 Hill-type muscle elements that represent core muscles of the shoulder girdle, including rotator cuffs, deltoids, serratus anterior, latissimus dorsi, among others [42]. In this study, the geometry of the model used was linearly scaled using the *OpenSim* geometric scaling tool then used to simulate all tasks. The subject's handheld load and hand mass was applied as a single mass at a point 3 cm distal to the wrist joint.

C. Muscle Redundancy Solver

Described by (1a), the RMR solver minimizes the sum of squared muscle activations at each time frame (static optimization), while adding a penalty on reserve actuators to ensure that motion is generated predominantly by muscles [33]. An equality constraint is imposed to match the measured $\ddot{q}$ and estimated $\hat{\ddot{q}}$ coordinate accelerations (1b), and the rate of change of muscle activation is restricted to respect the physiological first-order activation dynamics (1c).

$$\min_{(a,c)} \sum_{i=1}^{N_m} w a_i^2 + \sum_{j=1}^{N_q} v c_j^2 \tag{1a}$$

$$\text{subject to match accelerations: } \ddot{q} = \hat{\ddot{q}} \tag{1b}$$

$$\text{maintain physiological bounds: } lb_i \leq a_i \leq ub_i \tag{1c}$$

where a_i is activation of muscle i, w is the weight assigned to activation of muscle i which is chosen as one for all muscles, c_j control input to reserve actuator j, v is the weight assigned to control of reserve actuator j which is always equal to ten, lb_i and ub_i are the lower and upper physiological activation bounds, respectively, of muscle i, as described by Belli et al. [33].

D. GH Stability Formulations

GH stability was formulated with different approaches, first as constraints that restrict the GH-JCF direction to lie within a specified perimeter, then instead by penalizing joint contact force directions in proportion to the deviation from a single point or from a defined perimeter (Fig. 1). In all formulations, the direction of the joint contact force vector $\vec{F}$ is described by the intersection point (o_p in Fig. 2, and Fig. 7 in Appendix I) of the force's line of action with the glenoid plane—the plane containing the glenoid cavity border. This intersection point is referred to here as the GH-JCF direction on the glenoid plane, with coordinates described by the position vector $\vec{p}_{gc}$, described by (15) in Appendix I.

1) Point: In this formulation, the GH-JCF is forced to intersect the point at the glenoid cavity center. Described by (2), this formulation forces the angle θ between $\vec{F}$ and the vector from the GH joint center to the glenoid cavity center (z_g axis) to be 0 (Fig. 2).

$$\theta = 0 \tag{2}$$

2) Circle: In the RMR solver, GH stability is formulated as an inequality constraint on the GH-JCF direction on the glenoid plane, preventing it from lying outside a circular stability perimeter with a center at glenoid cavity center. We chose the diameter of this circle D such that the perimeter characterizes a stability limit of 0.5. A stability limit of 0.5 is chosen within the reported ranges of empirical stability limits

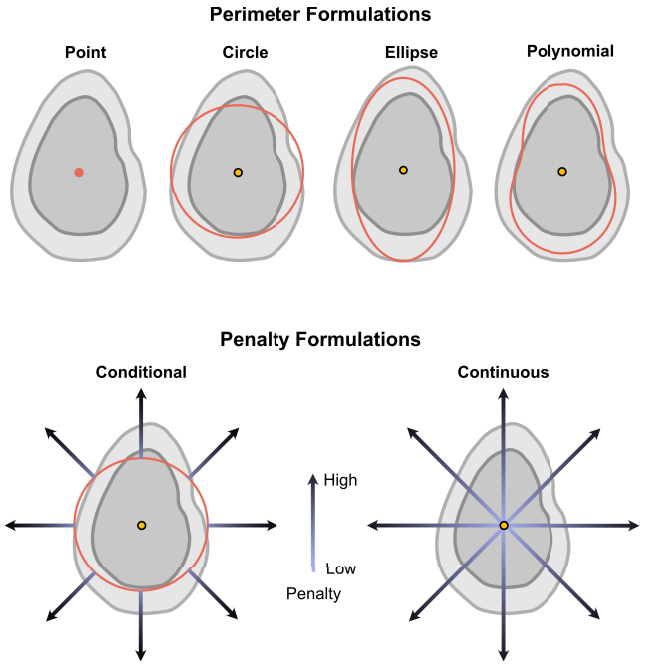

Fig. 1. Demonstration of GH stability formulations. Image of glenoid cavity and the different perimeters for GH stability formulations investigated, not necessarily drawn to scale. The polynomial shape is fit through 8 discrete points reported from concavity compression tests [6].

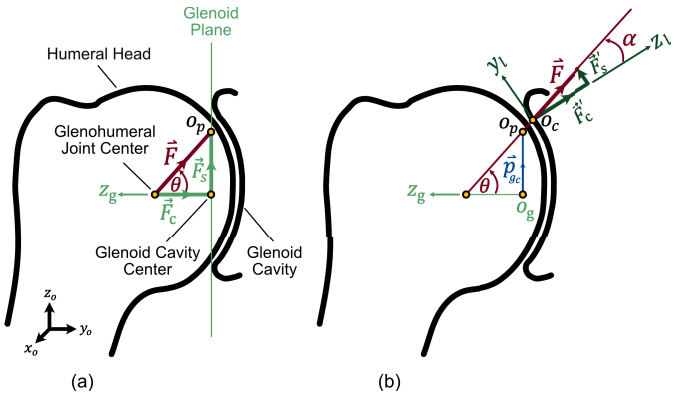

Fig. 2. GH-JCF decompositions. Illustration of the GH-JCF vector $\vec{F}$. Two decompositions of $\vec{F}$ are demonstrated. (a) $\vec{F}$ is decomposed onto the glenoid plane as a compressive component $\vec{F}_c$ in the direction of the z_g – *axis* and a shear component $\vec{F}_s$ normal to the z_g – *axis*. (b) $\vec{F}$ is decomposed as a compressive component $\vec{F}'_c$ in the direction z_l normal to the curve, and a shear component $\vec{F}'_s$ along y_l in the direction tangent to the curve.

(0.32−0.6) [7], [43]. The Circle formulation is described by (3).

$$\left(\frac{2\|\vec{p}_{gc}\|}{D}\right)^2 - 1 \leq 0 \tag{3}$$

where, $\vec{p}_{gc}$ is a position vector that describes the direction of the GH-JCF on the glenoid plane (Fig 7, and (15) in Appendix I). Note that, the stability limit is a dimensionless quantity however, $\|\vec{p}_{gc}\|$, and D have the dimension of length.

3) Ellipse: In this formulation, the direction of the GH-JCF is constrained to stay within an elliptical perimeter, with a long axis in the superior-inferior direction and short

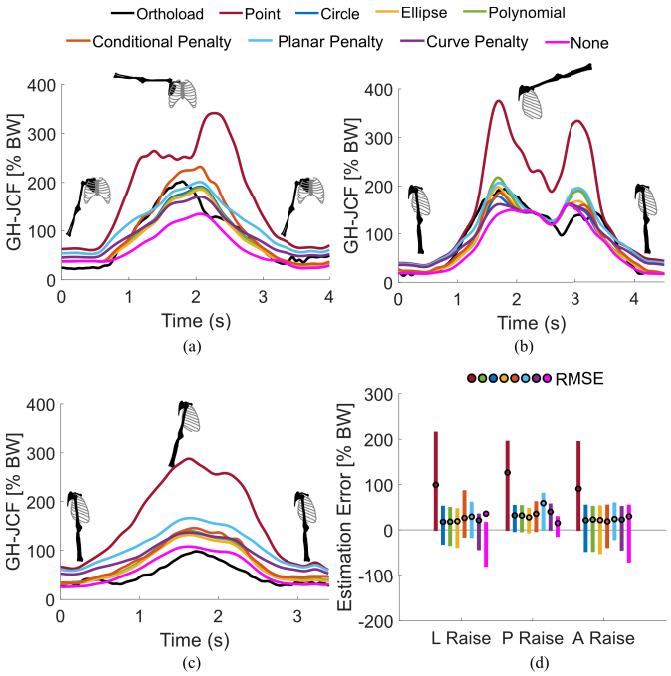

Fig. 3. Estimated GH-JCF magnitude vs *in vivo* measurements. (a) - (c) GH-JCF vector magnitude as a percentage of the body weight (%BW) in all tasks with the different stability formulations. (d) Estimation error in GH-JCF magnitude compared to *in vivo* measurements. Bars show the maximum positive (overestimation) and minimum negative (underestimation) errors. Circles indicate the root mean square error (RMSE) between the measured and estimated magnitudes throughout each task. L Raise (Lateral Raise) P Raise (Posterior Raise), A Raise (Anterior Raise).

axis in the anterior-posterior direction (Fig. 1), as per previous studies [11], [13]. Equation (4) describes the inequality constraint that formulates the Ellipse model.

$$\left(\frac{\|\vec{F}_{si}\|}{a\|\vec{F}_c\|}\right)^2 + \left(\frac{\|\vec{F}_{ap}\|}{b\|\vec{F}_c\|}\right)^2 - 1 \leq 0 \tag{4}$$

where $a = 0.61$ and $b = 0.34$ are the long and short axes of the ellipse that represent the empirical stability limits observed in concavity compression tests [6]. $\|\vec{F}_c\|$ is the magnitude of the compressive component of the estimated GH-JCF that acts perpendicular to the glenoid plane (Fig. 2, and Fig. 7 in Appendix I). $\|\vec{F}_{si}\|$ is the magnitude of the estimated shear force $\vec{F}_s$ in the superior-inferior direction, and $\|\vec{F}_{ap}\|$ is the magnitude of $\vec{F}_s$ in the anterior-posterior direction. The shear force $\vec{F}_s$ is the component of the estimated GH-JCF parallel to the glenoid plane.

4) Polynomial: In this formulation, the stability perimeter is defined by a 6th order polynomial fit of the empirical values reported from concavity compression experiments [6] (Fig. 1). The formulation is implemented as an inequality constraint described by (5).

$$\frac{r_{sc}^2}{L^2(\beta)} - 1 \leq 0 \tag{5}$$

where $L(\beta)$ is a 6^{th}-order polynomial fit of the empirical stability limits reported by concavity compression tests (Fig. 1) [6], and β is the radial angle in the glenoid plane from the center (Fig. 7 in Appendix I). Described by (6), planar

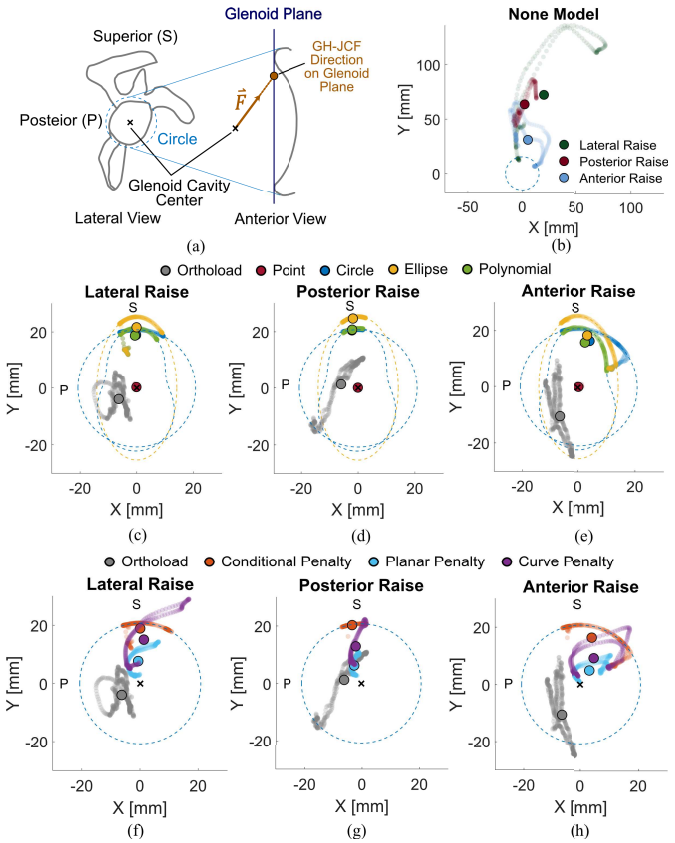

Fig. 4. Estimated GH-JCF direction vs *in vivo* measurements. Direction of the GH-JCF vector on the glenoid plane during all tasks, measured *in vivo* and estimated with the different stability formulations. (a) Lateral and anterior views of the scapula, with the Circle stability perimeter illustrated for scale, (b) GH-JCF direction on the glenoid plane with no stability formulation (None). (c)-(e) GH-JCF direction on glenoid plane from different perimeter formulations. (f)-(h) GH-JCF direction on glenoid plane with the different penalty formulations. Circles show the mean projection during each task. Dotted lines represent the different stability perimeters of each stability formulation.

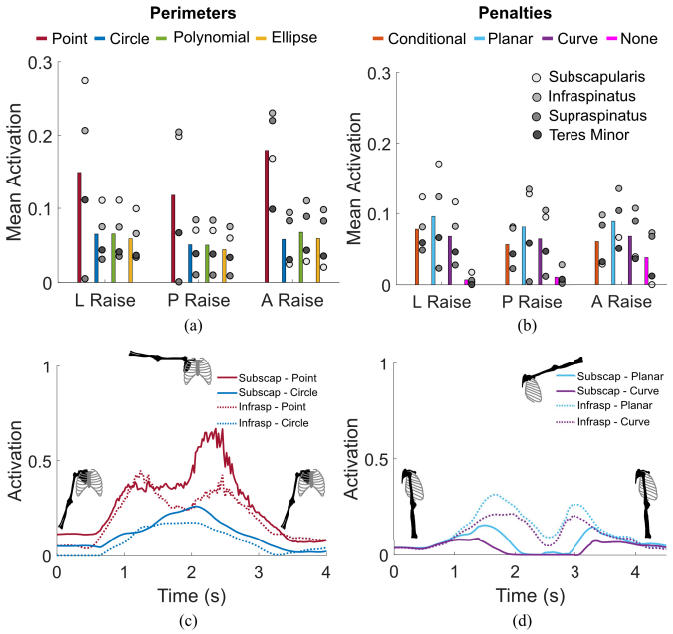

Fig. 5. Estimated rotator cuff activation. (a), (b) Mean activation of the rotator cuff muscles group in all tasks with the perimeters and penalties formulations. Circles show the mean activation of each individual muscle throughout each task. Bars show the mean activation of all muscles. (c), (d) Activation of selected rotator cuff muscles with different stability formulations in lateral and anterior raise tasks. Subscap (Subscapularis), Infrasp (infraspinatus).

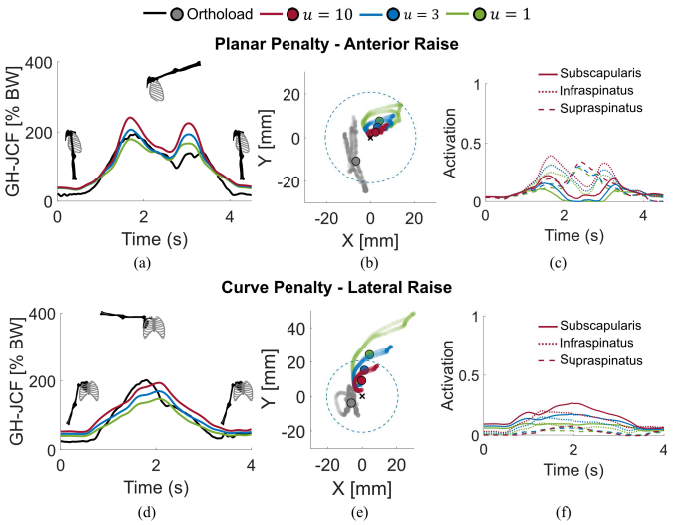

Fig. 6. Sensitivity analysis. Estimated joint contact forces, GH-JCF direction on the glenoid plane, and activation of the rotator cuff muscles in anterior raise task with the Planar Penalty formulation (top row), and in lateral raise task with the Curve Penalty formulation (bottom row), for varying penalty weights u in the cost function. (a), and (d) show the GH-JCF magnitude. (b), and (e) GH-JCF direction on the glenoid plane. Circles show the mean of the GH-JCF direction on the glenoid plane over time; light shades show the trajectory of the GH-JCF direction with time; dotted lines represent the Circle stability border. (c), and (f) Activation of the rotator cuff muscles.

shear-to-compressive ratio r_{sc} is the ratio between the shear and compressive components of $\vec{F}$ decomposed parallel and normal to the glenoid plane (Fig. 2).

$$r_{sc} = \frac{\|\vec{F}_s\|}{\|\vec{F}_c\|} = \tan\theta \tag{6}$$

5) Conditional Penalty: In this formulation, a penalty is added as a cost in the objective function if the GH-JCF direction crosses the circular stability perimeter (Fig. 1), again defined with radius that corresponds to a stability limit of 0.5. The penalty term is applied proportional to the planar shear-to-compressive ratio r_{sc} squared (6). The objective function in the original formulation (1a) is thus replaced by (7).

$$\min_{(a,c)} \sum_{i=1}^{N_m} w_i a_i^2 + \sum_{j=1}^{N_q} v_j c_j^2 + uN \tag{7}$$

where u is the penalty weight, set a value of three, and N is a penalty term defined as follows,

$$N = \begin{cases} 0 & r_{sc} < 0.5 \\ r_{sc}^2 & r_{sc} \geq 0.5 \end{cases} \tag{8}$$

6) Continuous Planar Penalty: In this formulation, a penalty term is added to the objective function continuously, proportionally penalizing the distance squared from the GH-JCF direction away from the center of the glenoid cavity. The penalty term is equal to the planar shear-to-compressive

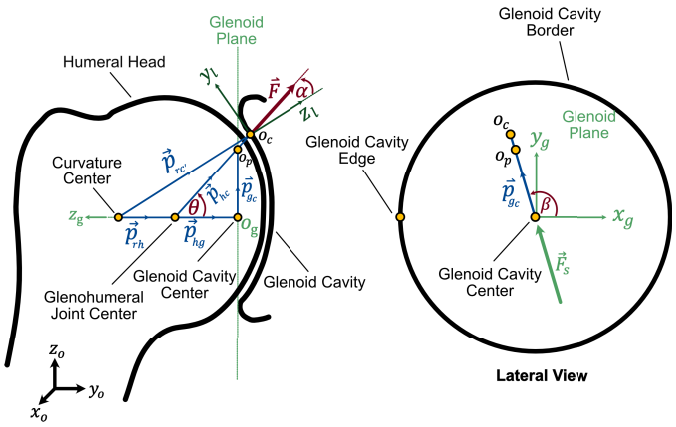

Fig. 7. Demonstration of the direction of the GH-JCF vector on the glenoid plane. Point o_p is the intersection of the line of action of $\vec{F}$ with the glenoid $x_g y_g$ plane. Axes x_g and y_g are the axes of the glenoid frame $o_g - x_g y_g z_g$ whose origin is at the glenoid cavity center (GCC).

ratio (6), and scaled by a weighting factor of $u = 3$. With the Planar Penalty formulation (9) replaces the original objective function in the RMR solver (1a).

$$\min_{(a,c)} \sum_{i=1}^{N_m} w_i a_i^2 + \sum_{j=1}^{N_q} v_j c_j^2 + u\ r_{sc}^2 \tag{9}$$

7) Continuous Curve Penalty: This formulation is similar to the Continuous Planar Penalty, but considers the shape of the glenoid cavity curvature by applying a penalty term that is equal to the curve shear-to-compressive ratio r'_{sc} (10). This ratio is defined as the magnitude ratio between the components of $\vec{F}$ tangent and normal to the glenoid cavity curvature (Fig. 2).

$$r'_{sc} = \frac{\|\vec{F}_{s'}\|}{\|\vec{F}_{c'}\|} = \tan\alpha \tag{10}$$

The curvature of the glenoid cavity was assumed to be circular with a radius and a center location that achieve specific height (4 *cm*) and depth (2 *mm*) of the glenoid cavity (Fig. 8 in Appendix I) based on *in vitro* morphological measurements [44]. With this formulation, the original objective function (1a) is replaced by (11). The penalty term in (11) scaled by a weighting factor of $u = 3$.

$$\min_{(a,c)} \sum_{i=1}^{N_m} w_i a_i^2 + \sum_{j=1}^{N_q} v_j c_j^2 + u\ r'^2_{sc} \tag{11}$$

8) None: Muscle redundancy was also solved with no inequality constraints or cost penalties stability formulations, referred to as the None model.

E. Simulation Pipeline

Inverse musculoskeletal simulations were performed on the *Orthoload* dataset using the geometrically scaled thoracoscapular model. Muscle redundancy was solved for all tasks with the RMR solver and the relevant GH stability formulation.

F. Model Validation

For each stability formulation, the estimated magnitudes and directions of the GH-JCFs for the three movements were compared to those measured by the instrumented joint prosthesis. Estimated GH-JCF magnitudes are presented as time series, normalized by body weight (BW), and their agreement with measured GH-JCFs is analyzed as average root-mean-square-error (RMSE) differences from the measured forces. Estimated GH-JCF direction was compared visually to the measured directions. Estimated muscle activations of the rotator cuff muscles are presented here in the context of how they may contribute to joint contact forces, but there is no available observed data with which to compare.

G. Sensitivity Analysis

Sensitivity analysis was performed to evaluate the effects of the stability limit value on the solution obtained from the perimeter formulations. A case study was performed on the Polynomial model by scaling up and down the size of the perimeter by a factor of 2, with results shown in Appendix I. The polynomial model was chosen as it represents a superset of the other perimeters that will illustrate how a perimeter model would generally respond to changes in perimeter size. Sensitivity analysis was also performed on the weights of the penalties in the objective function in the penalty formulations; weights were assigned $u = 1$, $u = 3$, and $u = 10$ in the RMR solver. The weight value determines how strongly the Curve or Planar penalty influences the objective function. In this analysis, we considered only the Curve Penalty formulation.

III. Results

A. GH-JCF Magnitude

With no stability formulation (None model), the overall pattern of the GH-JCF magnitude was similar to the measured force in all tasks (Fig. 3). Predicted peaks were, however, occasionally temporally shifted, particularly in lateral and anterior raises. In lateral and anterior raises, the None model underestimated the magnitude over the majority task duration, most notably in lateral raise. In posterior raise, however, the None model reproduced high magnitudes compared to the *in vivo* measurements most of the time.

The perimeter formulations predicted GH-JCF magnitudes with varying amounts of agreement with the in vivo measurements; RMSE of force magnitudes were between 15 – 126% BW. Some formulations predicted an offset in the timing of the peak force. With any perimeter formulation, predicted magnitude agreed better with the measurements than the None model in lateral and anterior raises. In posterior raise, however, all stability formulations overestimated force magnitude, wherein the perimeter models overestimated more than the None model. In all tasks, the Point model overestimated the GH-JCF magnitude the most, with RMSE approximately 100% BW in lateral raise, 126% BW in posterior raise, and 91% BW in anterior raise compared to the measured force magnitudes. Other perimeter models estimated force magnitudes with RMSE approximately around 18% BW in

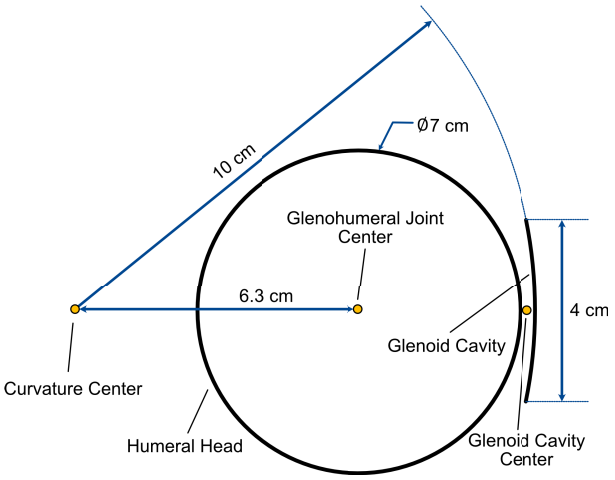

Fig. 8. Geometry of the glenoid cavity curvature used in the Curve Penalty formulation. The glenoid cavity center is first found by placing a model marker roughly in the same plane of the glenoid cavity border on the mesh geometry. The height of the glenoid cavity is set equal to 4*cm* based on morphological measurements from *in vitro* experiments [44]. Then a circle is constructed such that its center is collinear with the glenohumeral joint center, and its radius achieve a glenoid cavity depth of 2*mm*—a value within the reported ranges from *in vitro* measurements [44]. The radius of the humeral head is constructed based on measurements from the model's mesh geometry.

lateral raise, 30% BW in posterior raise, and 22% BW in anterior raise.

The penalty formulations predicted GH-JCF profiles similar to the perimeter formulations in all tasks, with somewhat higher RMSEs, most notably in posterior raise with the Planar Penalty (59% BW). In lateral and anterior raise, RMSEs with the penalty formulations were approximately 25% BW, and 21% BW, respectively.

Among all stability models, predictions with the lowest RMSEs were computed with the Circle model in lateral raise (≈ 18% BW), the None model in posterior raise (≈ 15% BW), and the Conditional Penalty model in anterior raise (≈ 19% BW).

B. GH-JCF Direction

During all tasks, the *in vivo* measured GH-JCFs were always directed inside the glenoid cavity, often slightly posteriorly, though not always (Fig. 4). Except for some time frames at the beginning and end of lateral and anterior raise tasks, with the None model, the GH-JCF direction was directed outside of the glenoid cavity—most notably up to 13 *cm* superior and 7 *cm* anterior to the glenoid in the lateral raise. With the Point formulation, the estimated GH-JCF was directed precisely at the glenoid cavity center. With the Circle, Ellipse and Polynomial formulations, the GH-JCF was directed near or directly along the superior perimeters throughout all tasks.

With the Conditional Penalty formulation, the GH-JCF direction was again often directed close to or along the superior perimeter. With the Continuous Penalty formulations, the GH-JCF direction intersected the glenoid more centrally in the glenoid, and agreed best with the *in vivo* measurements, wherein estimations with the Planar Penalty matched slightly better than with the Curve Penalty.

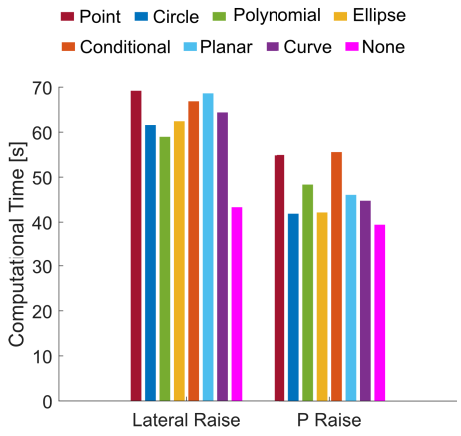

Fig. 9. Computational time taken by the RMR solver to solve the entire task for each stability formulation in lateral and anterior raise tasks.

C. Rotator Cuff Muscle Activation

Estimated rotator cuff muscle activations were notably higher with any stability formulation than in the None model (Fig. 5), with highest activations from the Point model. In all tasks, activation was higher with the penalty models than with any of the shape perimeter models. Among the penalty models, rotator cuff activations were higher in all tasks with the Planar model.

Activation levels of the rotator cuff muscles varied between tasks. In the lateral raise, the subscapularis muscle had the highest activation with all stability models, followed by the infraspinatus and the teres minor. In the posterior raise, the infraspinatus muscle had the highest activation, followed by the subscapularis and the teres minor with all stability model except the Conditional Penalty model where the subscapularis came first. In the anterior raise, the infraspinatus muscle had the highest activation, followed by the supraspinatus and the teres minor with most of the stability models. Activation patterns also varied across stability formulations. In the anterior raise, the teres minor muscle was the least activated muscle with the Point, the Curve Penalty and the Planar Penalty models, and was the third most activated with all other models.

D. Computational Efficiency

Computational efficiency on an Acer Predator Triton 500 SE laptop with Core i7-11800H processor varied with stability models (Fig. 9 in Appendix I). In lateral raise for example, computational time ranged from 43.2 seconds for the None model to 69.1 seconds for the Point model. In the posterior raise, times ranged from 39.2 seconds to 54.8 seconds. Overall, differences in computational time between perimeter and penalty formulations remained within 15 seconds.

E. Sensitivity Analysis

We evaluated the sensitivity of the solutions reproduced by the different formulations to the size of the stability perimeter and the value of the optimization weight u (Fig. 6, and Fig 10 in Appendix I). Results showed that reducing the diameter of the stability perimeter resulted in stricter predictions

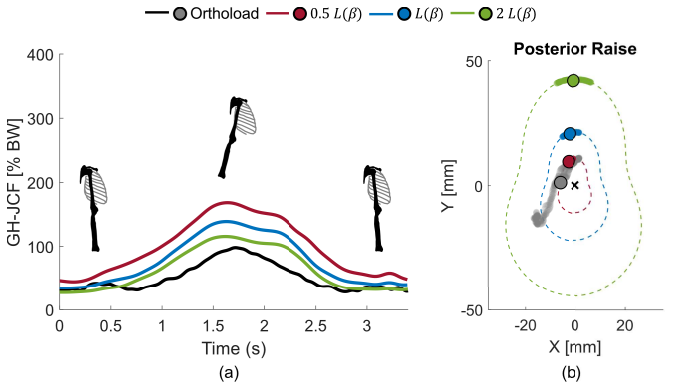

Fig. 10. Estimated GH-JCF magnitude (a), and direction on the glenoid plane (b) in posterior raise task with the Polynomial formulation, for varying sizes of the stability perimeter. Circles show the mean of the GH-JCF direction on the glenoid plane over time; light shades show the trajectory of the GH-JCF direction with time; dotted lines represent the Polynomial stability border.

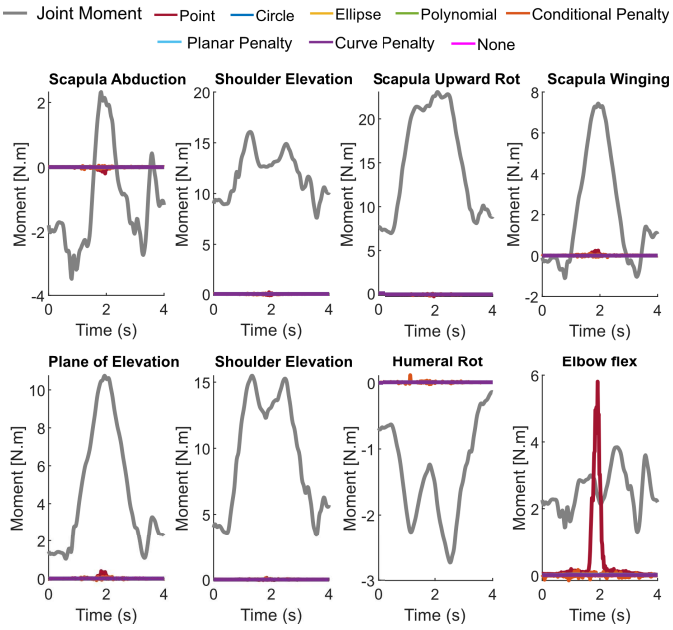

Fig. 11. Moments of the scapulothoracic joint and the GH joint compared to moments of reserve actuators with the different stability formulations in lateral raise task. Reserve actuator moments were negligible except with the Point model in elbow flexion.

with an increased GH-JCF magnitude and closer direction to the glenoid cavity center, whereas increasing the diameter of the stability perimeter had the opposite effect. Likewise, increasing the optimization weight led to a higher GH-JCF magnitude and closer direction to the glenoid cavity center, while decreasing it resulted in a lower GH-JCF magnitude with a direction farther from the glenoid cavity center. It was simultaneously observed that, by reducing the size of the stability border and increasing the optimization weight, the activation of the rotator cuff muscles increased, and vice versa.

IV. Discussion

In this study, we investigated different approaches to model GH stability in musculoskeletal simulations using the

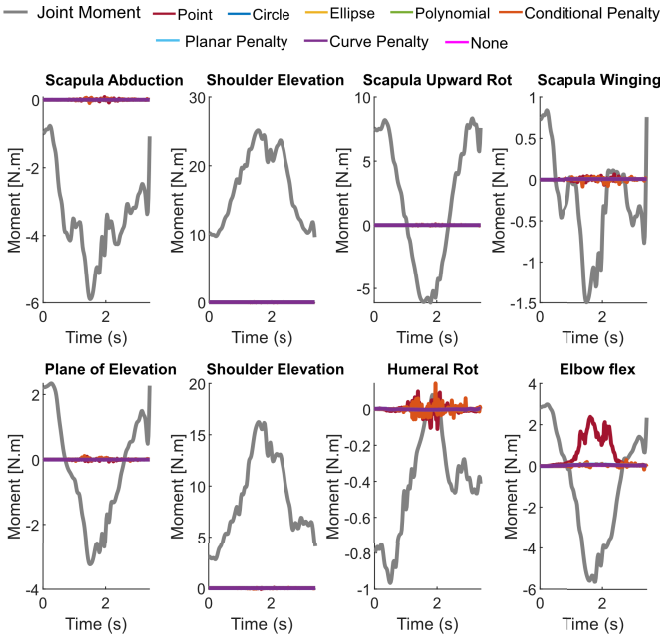

Fig. 12. Moments of the scapulothoracic joint and the GH joint compared to moments of reserve actuators with the different stability formulations in posterior raise task. Compared to the joint moments, reserve actuator moments were negligible ensuring movement generated by muscles. Only with the Point model, the elbow flexion reserve actuator moment was considerably high compared to the elbow flexion moment.

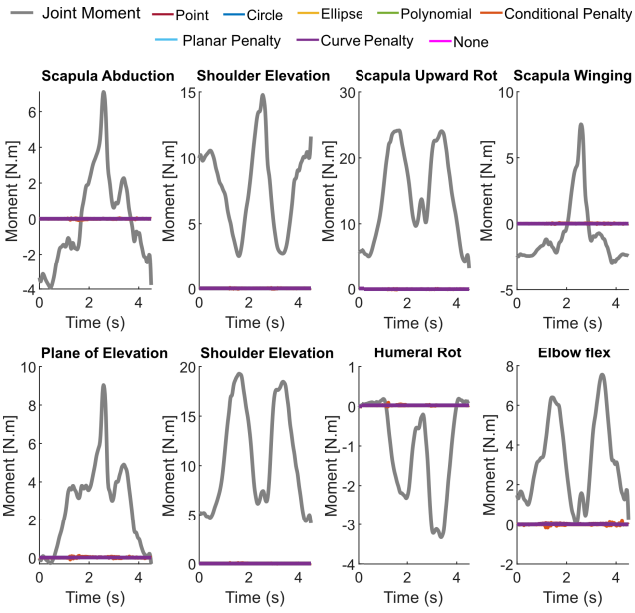

Fig. 13. Moments of the scapulothoracic joint and the GH joint compared to moments of reserve actuators with the different stability formulations in Anterior raise task. Compared to the joint moments, reserve actuator moments were negligible ensuring movement generated by muscles.

thoracoscapular shoulder model and the RMR solver. The thoracoscapular *OpenSim* model incorporates a validated model of the scapulothroacic articulation. The RMR solver includes a formulation of the GH stability that can be customized. Both are freely available. The goal of this investigation was

to determine which GH stability formulations most faithfully reproduced GH-JCF magnitude and direction measured with an instrumented shoulder prosthesis.

Existing formulations of GH stability have either shown limited accuracy or lack quantitative validation. We quantitatively investigated and tested different GH stability formulations via two general schemes—incorporating inequality constraints that constrain the GH-JCF direction to different perimeters, and introducing penalties in the objective function that allow but penalize GH-JCF directions that deviate from the glenoid cavity center.

When a stability condition was enforced, activation of the rotator cuff muscles increased notably compared to the None formulation, which is consistent with the findings of Belli et al. [33]. In contrast to findings from nerve-blocking studies, which suggested that the supraspinatus muscle plays an important role in shoulder abduction [45], our results indicate a lower contribution of the supraspinatus to this motion. Interestingly, this outcome is consistent with earlier simulations using the Delft shoulder model, where supraspinatus activation during arm abduction was reported to be minimal, while the subscapularis muscle was found to be more substantially involved [13]. To directly validate these model-based observations, fine-wire EMG recordings would be highly valuable; however, such measurements were not available in the Orthoload dataset used in this study.

Estimated GH-JCFs without any GH stability formulation (None) were lowest in magnitudes and directed several centimeters above the glenoid cavity during the three tasks. This would imply that the humerus would no longer be supported by the glenoid cavity but only by soft tissues, which has not been observed experimentally. With the strictest stability formulation (Point), that forced the estimated GH-JCF to be directly in the center of the glenoid cavity, GH-JCF magnitudes were overestimated by up to 2 times body weight during the movements, achieved by excessive muscle activations and co-contractions. This formulation can thus also be considered inaccurate.

Constraining the GH-JCF direction within specified perimeters using inequality constraints estimated GH-JCF that, though closer to the glenoid than with no constraints, still did not agree with those measured experimentally; they were instead nearly always directed along the superior perimeter, and can likewise be considered unrealistic. The Conditional Penalty formulation was constructed as a sort of compromise, as it allowed GH-JCF to be directed outside of the defined perimeter, but at an additional cost in the objective function. However, largely the same behavior was found; GH-JCF direction was still directed very close to or along the superior perimeter throughout most of the activities, so it can also be considered inaccurate.

The Continuous Penalty formulations have no specified perimeter or border, but instead encourage the GH-JCF to be directed centrally in the glenoid cavity, achieved by penalizing the GH-JCF direction that deviates from the glenoid cavity center, equally in all directions. These formulations estimated GH-JCF magnitudes that differed from measured forces by up to 59% BW, but the estimated GH-JCF directions agreed rather well to those measured in vivo. They also encouraged enough muscle co-contraction of particularly the rotator cuff muscles to achieve GH stability, though no fine wire EMG data was available in the Orthoload data set for a direct comparison. Taking into account the curvature of the glenoid cavity (Curve penalty) vs. simplifying the glenoid to a plane (Planar penalty) did not result in substantially more accurate GH-JCF magnitudes or directions, suggesting that the more simplified geometric model in the muscle redundancy solver may suffice.

Interestingly, in the posterior raise, GH-JCF magnitude was overestimated across all stability formulations, most notably under the strictest one, while the None formulation provided the closest prediction. This overestimation may reflect reduced GH translation in the implant, or a lower sensitivity to GH translation following surgery, which could decrease the need for muscle co-contraction. Additionally, rigid mechanics likely overestimate reaction loads, as translations that would normally be resisted by muscle and ligament stretch are instead borne by reaction forces of the spherical joint. Similar observations in similar arm positions have been reported in previous validation studies using different shoulder models [37], [46]. Future work incorporating fine-wire EMG data may provide valuable insights into this.

Estimated GH-JCF directions were most accurate with the two Continuous Penalty formulations, though did not entirely match the *in vivo* measurements given that modeling requires a number of simplifications and assumptions. First, the modeled GH joint is simplified; it ignores humeral head translation and the effect of the glenoid labrum on stabilizing the GH joint. *In vitro* studies showed that GH stability is spatially dependent on the point of contact between the humeral head and the glenoid cavity as well as on the thickness of the glenoid labrum at that point [6], [7]. Inverse simulation using skin markers measurements is furthermore not likely suitable to accurately reproduce humeral head translation, which is on the same order of magnitude of measurement errors arising from soft tissue artifacts, particularly in scapular movement [47], [48]. Second, while simulations were performed with a geometrically scaled model, additional scaling based on muscle strength might have improved model predictions. This, however, was not possible in the current study, as no information about the subject's strength was available in the dataset, nor was fine wire EMG data. Third, the subject underwent a shoulder hemiarthroplasty, so his joint topology and musculoskeletal system will not precisely match even a scaled model.

With the Curve Penalty model, the predicted direction of the GH-JCF on the glenoid plane was slightly further from the glenoid cavity center than with the Planar Penalty model. This is because the shear force magnitude decomposed tangent to the glenoid curve is always less than or equal to the shear force magnitude projected onto the glenoid plane. This means that the penalty term in the Curve Penalty formulation will be smaller than in the Planar Penalty formulation for any non-zero angle θ and similar weight u, and the Curve Penalty formulation will predict less co-contraction. It is, however, worth mentioning that the two models can equivalently lead

to the same behavior by tuning the weight of the penalty term u, as was indicated in the sensitivity analysis.

The GH-JCFs have been estimated via inverse musculoskeletal simulation in a few published studies, one using the OpenSim version of the Delft shoulder model [49] and another other using the Newcastle shoulder model, which defined muscles similarly to the Delft model [19]. In both of these studies, the estimated GH-JCFs were directed within the glenoid cavity, even without applying any shoulder stability models. These findings contradict previous findings by van der Helm who, using the Delft shoulder model, reported that a stability perimeter was necessary in tasks like lateral and anterior raise [50]. It is worth mentioning that the musculoskeletal models used in these studies characterized joints and muscles slightly differently than the thoracoscapular model in the current study. Future work can investigate this issue by testing the proposed stability formulations on the OpenSim version of the Delft and/or Newcastle shoulder models.

Some other limitations exist with this study. The participant underwent a surgery that sacrificed the joint capsule, so it is likely that greater than normal muscle forces were required to compensate for the absence of the capsule's stabilizing effect. This limitation is unavoidable in this gold standard method validation, as it requires surgical implantation of an instrumented joint prosthesis. Data measured *in vivo* that includes both forces and fine-wire EMG of deep muscles would be of some use in further validation studies, but to the best of our knowledge, no such data exists.

The subject had a prosthetic humeral head but an intact glenoid, likely altering the GH joint geometry and muscle moment arms. These geometric changes were not accounted for and may have influenced the predictions, though likely to a minor extent. For the perimeter formulations, the GH-JCF direction is always constrained to the defined perimeter, as confirmed by the sensitivity analysis; even when the perimeter diameter was larger or smaller, the GH-JCF direction remained on the perimeter. Similarly, in Continuous Penalty formulations, the formulation will still penalize deviations of the GH-JCF direction proportionally from the glenoid cavity center. Even with more personalized models of muscle moment arms, discrepancies between measured and predicted values would likely exist due to model simplifications. While GH-JCF magnitudes might also depend on geometric variations, the overall pattern and trends would likely remain consistent, closely approximating measured values. Also, data from only one subject was used for model validation; inter subject data is needed to better shape the continuous penalty approach, but it is already clear that the perimeter formulations have undesirable/unrealistic characteristics.

It should also be noted that some gap filling of marker trajectories in the Orthoload dataset was required. These gaps were interpolated using a spline fit, which sometimes introduced artifacts, particularly in trunk markers at the beginning or end of movements. To minimize these effects, affected markers were either disregarded when possible or assigned lower weights in the inverse kinematics solution.

Future model improvements should include adding ligaments to the model, and improving muscle geometry models of the biceps and triceps, particularly for activities that involve elbow flexion. In the current model, biceps and triceps muscles do not have a wrapping point/surface around the elbow joint and are thus only suited for tasks with an extended elbow.

V. Conclusion

This work comprehensively explored different formulations of GH stability in inverse musculoskeletal simulations using the thoracoscapular shoulder model and the rapid muscle redundancy solver. Estimates of GH-JCF direction and magnitude with the different stability formulations were tested against *in vivo* measurements. All stability formulations predicted the GH-JCF magnitude with relatively comparable accuracy, except for the strictest Point formulation, which constrained the joint contact force direction to the center of the glenoid cavity and overestimated the JCF magnitude. Continuous penalty formulations that penalized deviations of the GH-JCF direction from the glenoid cavity center predicted GH-JCF direction more accurately than the other models, estimating GH-JCF within, rather than along or outside of, the glenoid cavity perimeter. These findings support the proposed continuous penalty stability formulations as benchmark methods for analyzing shoulder loading, providing a more adequate and reasonable description of GH stability.

Appendix I
Supporting Information

A. Glenohumeral Joint Contact Force Direction

The glenohumeral joint contact force (GH-JCF) is a sliding vector ($\vec{F}$ in Fig. 7) that passes through the center of the glenohumeral (GH) joint, coincident with the center of the humeral head at any instant in time. The line of action of $\vec{F}$ intersects with the glenoid cavity at a point. This point characterizes the GH-JCF direction in the glenoid cavity. The direction of $\vec{F}$ is used as a metric to assess the GH stability. The GH joint is stable as long as the direction of $\vec{F}$ is within the glenoid border. Ideally, the intersection point of $\vec{F}$ with the glenoid cavity curvature (point o_c in Fig. 7) should lie on the articular surface of the glenoid. We, however, approximate this point by taking the intersection of line of action with the glenoid plane (point o_p in Fig. 7). The glenoid plane is the plane containing the border of the glenoid cavity. To construct the glenoid plane ($x_g y_g$ plane in Fig. 7), a virtual marker was first positioned at the modeled GH joint center—defined according to the ISB standard [27], [41]. The glenoid cavity center and one point along the glenoid edge were then visually identified on the mesh geometry of the scapula in the model, and virtual markers were placed at these locations. Using these three virtual markers, the glenoid reference frame $o_g - x_g y_g z_g$ was defined as follows:

- o_g: at the glenoid cavity center,
- z_g: from glenoid cavity center to the GH joint center,
- x_g: normal to z_g and lies in the plane containing the humeral head center, the glenoid cavity center and the glenoid cavity edge,
- y_g: normal to x_g and z_g.

The coordinates of the intersection point o_p on the glenoid plane (i.e., GH-JCF direction on the glenoid plane) can be described by a vector $\vec{p}_{gc}$, where $\vec{p}_{gc} = \vec{p}_{hc} - \vec{p}_{hg}$. Vector $\vec{p}_{hg}$ is the position vector from the GH joint center to the glenoid cavity center, and $\vec{p}_{hc}$ is the position vector from the GH joint center to the intersection point o_p. The position vector $\vec{p}_{hc}$ can be found as,

$$\vec{p}_{hc} = \frac{\|\vec{p}_{hg}\|}{\cos\theta} R\hat{F} \tag{12}$$

where, $\|\vec{p}_{hg}\|$ is the distance from the GH joint center to the glenoid cavity center, $\hat{F}$ is a unit vector along $\vec{F}$ found as $\hat{F} = \frac{\vec{F}}{\|\vec{F}\|}$, and θ is the angle between $\vec{F}$ and $\vec{p}_{hg}$ found as follows,

$$\theta = \cos^{-1}\left(\frac{\vec{F}\cdot\vec{p}_{gh}}{\|\vec{F}\|\ \|\vec{p}_{gh}\|}\right) \tag{13}$$

The matrix R is the rotation matrix that transforms from the global frame $o - x_o y_o z_o$ to the glenoid frame $o_g - x_g y_g z_g$. The rotation matrix R is defined as,

$$R = \left[\ x_{g,o}\ y_{g,o}\ z_{g,o}\ \right]^T \tag{14}$$

where $x_{g,o}$, $y_{g,o}$, and $z_{g,o}$ are the unit vectors of the glenoid frame $o_g - x_g y_g z_g$ defined in the global frame $o - x_o y_o z_o$. The direction of $\vec{F}$ on the glenoid plane expressed in $o_g - x_g y_g z_g$ is, thus, described by the position vector $\vec{p}_{gc}$ as follows,

$$\vec{p}_{gc} = R\left(\frac{\|\vec{p}_{hg}\|}{\cos\theta}\ \hat{F} - \vec{p}_{hg}\right) \tag{15}$$

B. Glenohumeral Contact Force Decomposition

Two decompositions of the GH-JCF namely the planar decomposition and the curve decomposition are introduced. The planar decomposition decomposes $\vec{F}$ into shear and compressive components of in the parallel and normal directions to the glenoid plane ($x_g y_g$ plane) respectively (Fig. 7). The shear force is the component of $\vec{F}$ in the glenoid plane $x_g y_g$ plane $\|\vec{F}_s\| = \|\vec{F}\|\sin\theta$, and the compressive force is the component of $\vec{F}$ perpendicular to the $x_g y_g$ plane $\|\vec{F}_c\| = \|\vec{F}\|\cos\theta$ (Fig. 7).

The curve decomposition decomposes $\vec{F}$ into two components $\vec{F}_{c'}$, and $\vec{F}_{s'}$ in the normal z_l and the tangent y_l directions to the curvature of the glenoid cavity at point o_c (Fig 7). Point o_c is the intersection of the line of action of $\vec{F}$ with the curvature of the glenoid cavity. We approximate the curvature of the glenoid cavity as a sphere with a radius $\|\vec{p}_{rc'}\|$ and a curvature center located on the z_g axis at a distance $d = \|\vec{p}_{rh}\|$ from the glenohumeral joint center. The radius of the curvature was chosen to achieve a specific height and width of the glenoid cavity (Fig. 8) based on *in vitro* morphological measurements [44].

The normal component of $\vec{F}$ to the curvature is defined as $\|\vec{F}_{c'}\| = \|\vec{F}\|\cos\alpha$, and the tangent component to the curvature is defined as $\|\vec{F}_{s'}\| = \|\vec{F}\|\sin\alpha$. Angle α is the angle between $\vec{F}$ and $\vec{p}_{rc'}$. $\vec{p}_{rc'}$ is the position vector from the curvature center to point o_c. The magnitude of $\vec{p}_{rc'}$ is equal to the radius of the curvature of the glenoid cavity. To find angle α, we apply the cosine law on angle θ' which is the supplementary angle of θ. Applying the cosine law on θ' results in a quadratic equation whose positive root is the length $\|\vec{p}_{hc'}\|$ as described in (16).

$$\begin{aligned}\|\vec{p}_{hc'}\| &= \|\vec{p}_{rh}\|\cos\theta' + \sqrt{(\|\vec{p}_{rh}\|\cos\theta')^2 - (\|\vec{p}_{rh}\|^2 - \|\vec{p}_{rc'}\|^2)}\end{aligned} \tag{16}$$

where $\vec{p}_{hc'}$ is the vector from the humeral head center to point o_c, and $\vec{p}_{rh}$ is the vector from the curvature center to the humeral head center. Angle θ is an exterior angle to the triangle whose sides are $\vec{p}_{hc'}$, $\vec{p}_{rc'}$, and $\vec{p}_{rh}$. Therefore, angle α can be computed as follows,

$$\alpha = \theta - \sin^{-1}\left(\frac{\|\vec{p}_{hc'}\|\sin\theta}{\|\vec{p}_{rc'}\|}\right) \tag{17}$$

C. Data Availability

Code and data used in this paper can be found at https://github.com/imihasan/customized-rmr-solver.

References

[1] H. E. J. Veeger and F. C. T. van der Helm, "Shoulder function: The perfect compromise between mobility and stability," *J. Biomechanics*, vol. 40, no. 10, pp. 2119–2129, Jan. 2007.

[2] J. Lucas, P. van Doorn, E. Hegedus, J. Lewis, and D. van der Windt, "A systematic review of the global prevalence and incidence of shoulder pain," *BMC Musculoskeletal Disorders*, vol. 23, no. 1, p. 1073, Dec. 2022, doi: 10.1186/s12891-022-05973-8.

[3] S. J. O'Brien, S. A. Taylor, P. N. Ramkumar, and A. E. White, "Developmental anatomy of the shoulder and anatomy of the glenohumeral joint," in *Rockwood Matsen's Shoulder*, 5th ed., C. A. Rockwood, F. A. Matsen, M. A. Wirth, S. B. Lippitt, E. V. Fehringer, and J. W. Sperling, Eds., Amsterdam, The Netherlands: Elsevier, 2017, ch. 1, pp. 1–33. [Online]. Available: https://www.sciencedirect.com/science/article/pii/B9780323297318000015

[4] L. F. Barnes, B. O. Parsons, S. B. Lippitt, E. L. Flatow, and F. A. Matsen, "Glenohumeral Instability," in *Rockwood Matsen's Shoulder*, 5th ed., C. A. Rockwood, F. A. Matsen, M. A. Wirth, S. B. Lippitt, E. V. Fehringer, and J. W. Sperling, Eds., Amsterdam, The Netherlands: Elsevier, 2017, ch. 13, pp. 543–649. [Online]. Available: https://www.sciencedirect.com/science/article/pii/B9780323297318000131

[5] L. M. Ladd, M. Crews, and N. A. Maertz, "Glenohumeral joint instability," *Clinics Sports Med.*, vol. 40, no. 4, pp. 585–599, Oct. 2021, doi: 10.1016/j.csm.2021.05.001.

[6] S. Lippitt and F. Matsen, "Mechanisms of glenohumeral joint stability," *Clin. Orthopaedics Rel. Res.*, vol. 291, pp. 20–28, Jun. 1993. [Online]. Available: https://journals.lww.com/clinorthop/fulltext/1993/06000/mechanisms_of_glenohumeral_joint_stability.4.aspx

[7] A. M. Halder, S. G. Kuhl, M. E. Zobitz, D. Larson, and K. N. An, "Effects of the glenoid labrum and glenohumeral abduction on stability of the shoulder joint through concavity-compression: An in vitro study," *J. Bone Joint Surgery-Amer. Volume*, vol. 83, no. 7, pp. 1062–1069, Jul. 2001.

[8] P. Westerhoff, F. Graichen, A. Bender, A. Rohlmann, and G. Bergmann, "An instrumented implant for in vivo measurement of contact forces and contact moments in the shoulder joint," *Med. Eng. Phys.*, vol. 31, no. 2, pp. 207–213, Mar. 2009.

[9] G. Bergmann et al., "In vivo gleno-humeral joint loads during forward flexion and abduction," *J. Biomechanics*, vol. 44, no. 8, pp. 1543–1552, May 2011.

[10] D. H. E. J. Veeger, F. van der Helm, and A. A. Nikooyan. (2023). *Kinematic and Kinetic Data Recorded With an Instrumented Shoulder Prosthesis*. [Online]. Available: https://data.4tu.nl/datasets/86db1d7d-13d9-4631-9c6b-1e3134a1ab38/1

[11] A. Kian et al., "Static optimization underestimates antagonist muscle activity at the glenohumeral joint: A musculoskeletal modeling study," *J. Biomechanics*, vol. 97, Dec. 2019, Art. no. 109348. [Online]. Available: https://www.sciencedirect.com/science/article/pii/S0021929019305718

[12] T. J. M. Dick et al., "Consensus for experimental design in electromyography (CEDE) project: Application of EMG to estimate muscle force," *J. Electromyogr. Kinesiol.*, vol. 79, Dec. 2024, Art. no. 102910.

[13] F. C. T. van der Helm, "A finite element musculoskeletal model of the shoulder mechanism," *J. Biomechanics*, vol. 27, no. 5, pp. 551–569, May 1994.

[14] E. K. Chadwick, D. Blana, R. F. Kirsch, and A. J. van den Bogert, "Real-time simulation of three-dimensional shoulder girdle and arm dynamics," *IEEE Trans. Biomed. Eng.*, vol. 61, no. 7, pp. 1947–1956, Jul. 2014.

[15] W. Wu, P. V. S. Lee, A. L. Bryant, M. Galea, and D. C. Ackland, "Subject-specific musculoskeletal modeling in the evaluation of shoulder muscle and joint function," *J. Biomechanics*, vol. 49, no. 15, pp. 3626–3634, Nov. 2016.

[16] K. R. Saul et al., "Benchmarking of dynamic simulation predictions in two software platforms using an upper limb musculoskeletal model," *Comput. Methods Biomechanics Biomed. Eng.*, vol. 18, no. 13, pp. 1445–1458, Oct. 2015.

[17] C. R. Dickerson, D. B. Chaffin, and R. E. Hughes, "A mathematical musculoskeletal shoulder model for proactive ergonomic analysis," *Comput. Methods Biomechanics Biomed. Eng.*, vol. 10, no. 6, pp. 389–400, Dec. 2007.

[18] K. R. S. Holzbaur, W. M. Murray, and S. L. Delp, "A model of the upper extremity for simulating musculoskeletal surgery and analyzing neuromuscular control," *Ann. Biomed. Eng.*, vol. 33, no. 6, pp. 829–840, Jun. 2005.

[19] I. W. Charlton and G. R. Johnson, "A model for the prediction of the forces at the glenohumeral joint," *Proc. Inst. Mech. Eng., H, J. Eng. Med.*, vol. 220, no. 8, pp. 801–812, Aug. 2006.

[20] S. R. Dubowsky, J. Rasmussen, S. A. Sisto, and N. A. Langrana, "Validation of a musculoskeletal model of wheelchair propulsion and its application to minimizing shoulder joint forces," *J. Biomechanics*, vol. 41, no. 14, pp. 2981–2988, Oct. 2008.

[21] M. Á. Ruiz-Ibán, J. A. Murillo-González, J. Díaz-Heredia, J. L. Ávila-Lafuente, and R. Cuéllar, "Pectoralis major transfer for subscapular deficiency: Anatomical study of the relationship between the transferred muscle and the musculocutaneous nerve," *Knee Surgery, Sports Traumatology, Arthroscopy*, vol. 21, no. 9, pp. 2177–2183, Sep. 2013.

[22] A. Kontaxis and G. R. Johnson, "The biomechanics of reverse anatomy shoulder replacement—A modelling study," *Clin. Biomechanics*, vol. 24, no. 3, pp. 254–260, Mar. 2009.

[23] S. Amrein, C. Werner, U. Arnet, and W. H. K. de Vries, "Machine-learning-based methodology for estimation of shoulder load in wheelchair-related activities using wearables," *Sensors*, vol. 23, no. 3, p. 1577, Feb. 2023. [Online]. Available: https://www.mdpi.com/1424-8220/23/3/1577

[24] R. Krishnan, N. Björsell, E. M. Gutierrez-Farewik, and C. Smith, "A survey of human shoulder functional kinematic representations," *Med. Biol. Eng. Comput.*, vol. 57, no. 2, pp. 339–367, Feb. 2019, doi: 10.1007/s11517-018-1903-3.

[25] B. Bolsterlee, D. H. E. J. Veeger, and E. K. Chadwick, "Clinical applications of musculoskeletal modelling for the shoulder and upper limb," *Med. Biol. Eng. Comput.*, vol. 51, no. 9, pp. 953–963, Sep. 2013.

[26] B. Bolsterlee, H. E. J. Veeger, and F. C. T. van der Helm, "Modelling clavicular and scapular kinematics: From measurement to simulation," *Med. Biol. Eng. Comput.*, vol. 52, no. 3, pp. 283–291, Mar. 2014.

[27] A. Seth, R. Matias, A. P. Veloso, and S. L. Delp, "A biomechanical model of the scapulothoracic joint to accurately capture scapular kinematics during shoulder movements," *PLoS ONE*, vol. 11, no. 1, Jan. 2016, Art. no. e0141028.

[28] A. Seth, M. Dong, R. Matias, and S. Delp, "Muscle contributions to upper-extremity movement and work from a musculoskeletal model of the human shoulder," *Frontiers Neurorobotics*, vol. 13, p. 90, Nov. 2019.

[29] D. G. Thelen and F. C. Anderson, "Using computed muscle control to generate forward dynamic simulations of human walking from experimental data," *J. Biomechanics*, vol. 39, no. 6, pp. 1107–1115, Jan. 2006.

[30] M. Praagman, E. K. J. Chadwick, F. C. T. van der Helm, and H. E. J. Veeger, "The relationship between two different mechanical cost functions and muscle oxygen consumption," *J. Biomechanics*, vol. 39, no. 4, pp. 758–765, 2006.

[31] Y. Blache, M. Begon, B. Michaud, L. Desmoulins, P. Allard, and F. Dal Maso, "Muscle function in glenohumeral joint stability during lifting task," *PLoS ONE*, vol. 12, no. 12, pp. 1–15, Dec. 2017, doi: 10.1371/journal.pone.0189406.

[32] D. C. McFarland, A. G. Brynildsen, and K. R. Saul, "Sensitivity of neuromechanical predictions to choice of glenohumeral stability modeling approach," *J. Appl. Biomechanics*, vol. 36, no. 4, pp. 249–258, Aug. 2020. [Online]. Available: https://journals.humankinetics.com/view/journals/jab/36/4/article-p249.xml

[33] I. Belli et al., "Does enforcing glenohumeral joint stability matter? A new rapid muscle redundancy solver highlights the importance of non-superficial shoulder muscles," *PLoS ONE*, vol. 18, no. 11, Nov. 2023, Art. no. e0295003.

[34] N. Rezzoug, A. Skuric, V. Padois, and D. Daney, "Simulation study of the upper-limb isometric wrench feasible set with glenohumeral joint constraints," *J. Biomechanical Eng.*, vol. 147, no. 2, Feb. 2025, Art. no. 024501, doi: 10.1115/1.4067329.

[35] C. Högfors, D. Karlssont, and B. Peterson, "Structure and internal consistency of a shoulder model," *J. Biomechanics*, vol. 28, no. 7, pp. 767–777, Jul. 1995.

[36] D. C. McFarland, E. M. McCain, M. N. Poppo, and K. R. Saul, "Spatial dependency of glenohumeral joint stability during dynamic unimanual and bimanual pushing and pulling," *J. Biomechanical Eng.*, vol. 141, no. 5, May 2019, Art. no. 024501.

[37] A. A. Nikooyan, H. E. J. Veeger, P. Westerhoff, F. Graichen, G. Bergmann, and F. C. T. van der Helm, "Validation of the Delft shoulder and elbow model using in-vivo glenohumeral joint contact forces," *J. Biomechanics*, vol. 43, no. 15, pp. 3007–3014, Nov. 2010.

[38] D. Lee, J. Lee, J. H. Oh, and C. S. Shin, "Effect of subscapularis repair on joint contact forces based on degree of posterior-superior rotator cuff tear severity in reverse shoulder arthroplasty," *Frontiers Bioeng. Biotechnol.*, vol. 11, pp. 1–13, Dec. 2023. [Online]. Available: https://www.frontiersin.org/journals/bioengineering-and-biotechnology/articles/10.3389/fbioe.2023.1229646

[39] Z. Chen et al., "Effect of rotator cuff deficiencies on muscle forces and glenohumeral contact force after anatomic total shoulder arthroplasty using musculoskeletal multibody dynamics simulation," *Frontiers Bioeng. Biotechnol.*, vol. 9, pp. 1–13, Jul. 2021. [Online]. Available: https://www.frontiersin.org/journals/bioengineering-and-biotechnology/articles/10.3389/fbioe.2021.691450

[40] C. G. M. Meskers, H. M. Vermeulen, J. H. de Groot, F. C. T. van der Helm, and P. M. Rozing, "3D shoulder position measurements using a six-degree-of-freedom electromagnetic tracking device," *Clin. Biomechanics*, vol. 13, nos. 4–5, pp. 280–292, Jun. 1998.

[41] G. Wu et al., "ISB recommendation on definitions of joint coordinate systems of various joints for the reporting of human joint motion—Part II: Shoulder, elbow, wrist and hand," *J. Biomechanics*, vol. 38, no. 5, pp. 981–992, May 2005.

[42] M. Millard, T. Uchida, A. Seth, and S. L. Delp, "Flexing computational muscle: Modeling and simulation of musculotendon dynamics," *J. Biomechanical Eng.*, vol. 135, no. 2, Feb. 2013, Art. no. 021005.

[43] S. B. Lippitt, J. E. Vanderhooft, S. L. Harris, J. A. Sidles, D. T. Harryman, and F. A. Matsen, "Glenohumeral stability from concavity-compression: A quantitative analysis," *J. Shoulder Elbow Surgery*, vol. 2, no. 1, pp. 27–35, Jan. 1993. [Online]. Available: https://www.sciencedirect.com/science/article/pii/S1058274609801341

[44] J. Wermers et al., "Glenoid concavity has a higher impact on shoulder stability than the size of a bony defect," *Knee Surgery, Sports Traumatology, Arthroscopy*, vol. 29, no. 8, pp. 2631–2639, Aug. 2021, doi: 10.1007/s00167-021-06562-3.

[45] S. P. McCully, D. N. Suprak, P. Kosek, and A. R. Karduna, "Suprascapular nerve block results in a compensatory increase in deltoid muscle activity," *J. Biomechanics*, vol. 40, no. 8, pp. 1839–1846, 2007. [Online]. Available: https://www.sciencedirect.com/science/article/pii/S0021929006002958

[46] M. Lavaill, C. Pizzolato, B. Bolsterlee, S. Martelli, and P. Pivonka, "Benchmark and validation of state-of-the-art muscle recruitment strategies in shoulder modelling," *Multibody Syst. Dyn.*, vol. 64, no. 1, pp. 105–120, May 2025, doi: 10.1007/s11044-024-09997-x.

[47] F. Dal Maso, M. Raison, A. Lundberg, A. Arndt, P. Allard, and M. Begon, "Glenohumeral translations during range-of-motion movements, activities of daily living, and sports activities in healthy participants," *Clin. Biomechanics*, vol. 30, no. 9, pp. 1002–1007, Nov. 2015.

[48] S. Konda, W. Sahara, and K. Sugamoto, "Directional bias of soft-tissue artifacts on the acromion during recording of 3D scapular kinematics," *J. Biomechanics*, vol. 73, pp. 217–222, May 2018.

[49] M. Lavaill, S. Martelli, K. Cutbush, A. Gupta, G. K. Kerr, and P. Pivonka, "Latarjet's muscular alterations increase glenohumeral joint stability: A theoretical study," *J. Biomechanics*, vol. 155, Jun. 2023.

[50] F. C. T. van der Helm, "Analysis of the kinematic and dynamic behavior of the shoulder mechanism," *J. Biomechanics*, vol. 27, no. 5, pp. 527–550, May 1994. [Online]. Available: https://www.sciencedirect.com/science/article/pii/0021929094900647